Supplementary Material

Dark-Field Imaging of Thin Specimens with a Forescatter Electron Detector at Low Accelerating Voltage

(Short title: Thin Specimens DF-FSED imaging at Low V_0)

Nicolas Brodusch, Hendrix Demers, and Raynald Gauvin

McGill University, Mining and Materials Engineering Department, Montréal, Québec, H3A 0C5 Canada

Corresponding author: Nicolas Brodusch, Mining and Materials Engineering Department, Wong building, McGill University, 3610 University Street, Montréal, Québec, H3A 0C5 Canada.

Email: nicolas.brodusch@mcgill.ca

Tel.: 514-398-7182, Fax: 514-398-4492.

S1. Description and Optimization of the DF-FSED Imaging System

The minimum collection angle α_1 and the maximum collection angle α_2 were selected by changing the detector distance (DD) and the working distance (WD) and were calculated, respectively, with the following equations:

$$\alpha_1 = \arctan\left(\frac{DD - a}{L + d - WD}\right) \qquad \text{(S1)}$$

$$\alpha_2 = \arctan\left(\frac{DD}{L + d - WD}\right) \qquad \text{(S2)}$$

where L is the camera screen dimension in the z direction, d is the distance from the pole piece to the upper edge of the camera screen and a is the diode width. The effective collection angle $\Delta\alpha$ was defined as $\Delta\alpha = \alpha_2 - \alpha_1$.

Figure S1 shows the effect of DD (Fig. S1a with a WD of 6 mm) and WD (Fig. S1b with a DD of 19 mm) on the collection angles of the bottom diodes of the FSED. The collections angles were calculated with equations (S1) and (S2). The system is completely described by α_1 and $\Delta\alpha$ ($\alpha_2 = \alpha_1 + \Delta\alpha$). The minimum angle α_1 increases when the WD and DD are larger. However, the increase rate was not the same for WD and DD. In contrast, the effective collection angle $\Delta\alpha$ exhibits a different trend for WD and DD. In Figure S1a, $\Delta\alpha$ decreases when the DD is larger, i.e., the effective collection angle is larger when the detector is close to the specimen. However in Figure S1b, first $\Delta\alpha$ increases when WD is increased, then reaches an apex at approximately 22 mm (i.e., α_1 = 48° approximately) and then decreases for longer WD. These results show that a wide range of α_1 value can be selected by changing the DD and WD with the DF-FSED imaging system. A small value of 34 mrad was calculated with a DD of 5 mm and WD of 6 mm. In our system, the EBSD camera was blocked by the cold trap anti-contaminator and the minimum DD achievable was only 18.7 mm (α_1 = 419 mrad). However, for safety, the minimum limit was set to 19 mm (α_1 = 426 mrad).

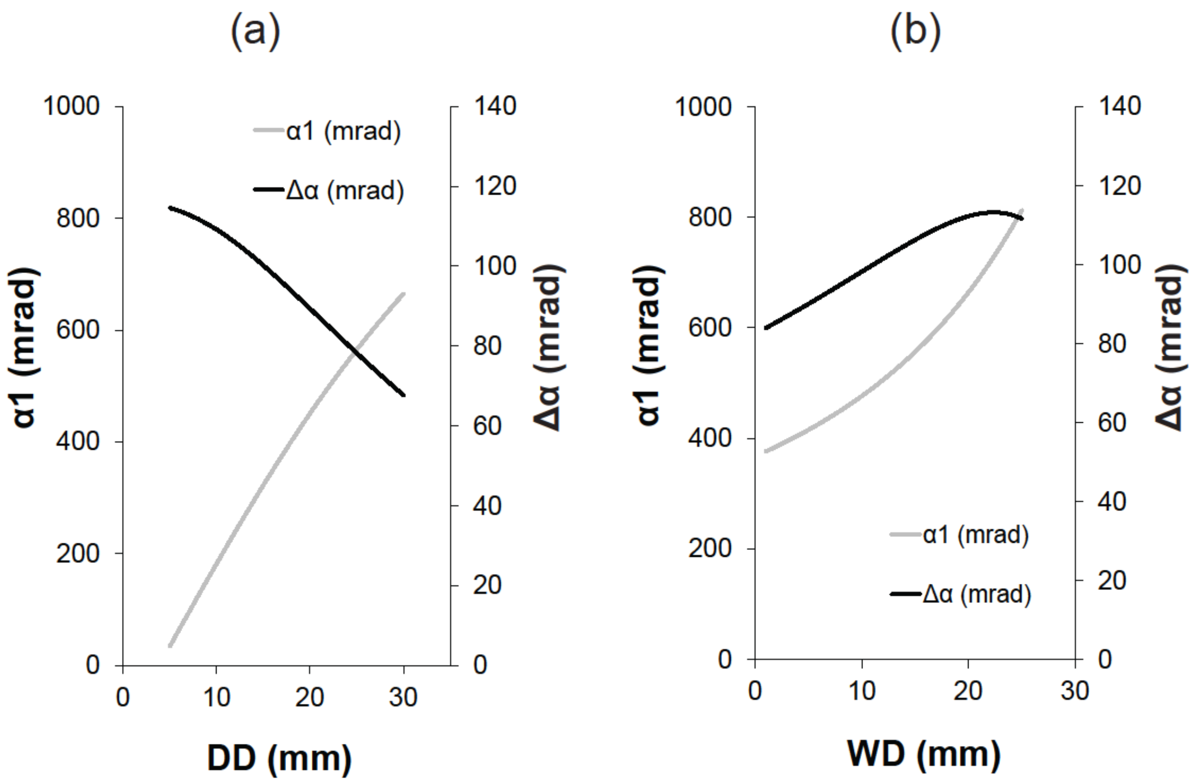

Supplementary Figure S1. Collection angles for the dark-field forescatter electron detector calculated with equations (S1) and (S2). Variation of the minimum collection angles (α_1) and the effective collection angle ($\Delta\alpha = \alpha_2 - \alpha_1$) as a function of (a) the detector distance (DD) with a working distance (WD) of 6 mm and (b) the WD with a DD of 19 mm.

Notwithstanding, these curves can be obtained on any EBSD system by simple calculations and the values of DD and WD allow the selection of the collection angles used for DF-FSED imaging. In our system, we used a DD of 19 mm and a short WD of 6 mm, this WD being the optimum value for BF-TE imaging in the SU-8000 CFE-SEM. The drawback is a small effective collection angle (α_1 and α_2 are 426 and 518 mrad, respectively, and $\Delta\alpha$ = 92 mrad). The minimum and maximum collection angles are higher than those in high accelerating voltage HAADF, but the effective collection angle is of the same order. However, the mean scattering angle at 30 kV is larger than at 200 kV for the same specimen thickness. High collection angles ensure that mostly only high angle elastic scattered electrons are collected without contribution of the diffracted beams (William & Carter 2009), which allows an almost pure *Z*-contrast imaging. For a high accelerating voltage STEM ADF system, the collection angles are determined by the camera length. For a DF-FSED system, the detector and working distances play a similar role than the camera length, the adjustment being optical for the STEM ADF system and geometrical for the DF-FSED system. Furthermore, the collection angles obtained for the DF-FSED system are comparable with those reported for other DF systems at low accelerating voltages (Morandi & Merli, 2007a & b; Felisari et al., 2011; Beyer et al., 2012).

S2. Spatial Resolution and Signal-to-Noise Ratio Calculations

Spatial resolution and signal-to-noise ratio were calculated with the SMART-J plug-in (Joy et al., 2000) in the ImageJ software (Rasband, 2012). All measurements were done without any image filtering and with a square region of interest (ROI) of 700 x 700 pixels except for the micrographs of Figures 3b and 3d where a ROI of 256 x 256 pixels was used. However, the spatial resolution measured with SMART-J is inaccurate when the original micrograph contains periodic or line structures (Joy, 2002; Probst et al., 2012). Another method was used to compare feature size observed in both BF-TE and DF-FSED micrographs. Line scans across a T_1 plate and Pt nanoparticles were done with ImageJ software. For each profile, the full width at half maximum (FWHM) was used to calculate the width or the nanoparticle diameter. For the Pt nanoparticles, four profiles with different orientations were extracted from the DF-FSED micrographs and the average diameter and standard deviation were calculated.

S3. Monte Carlo Modeling

The Monte Carlo simulations were carried out using the program CASINO version 3.2 (Demers, et al., 2010; Demers, et al., 2011). The software included the ELSEPA elastic electron scattering cross section (Salvat, et al., 2005). The simulation of high accelerating voltage STEM images was calibrated using experimental data (de Jonge, et al., 2010; Demers, et al., 2010). In this work, the channeling and diffraction effects were not taken into account in the simulations. The simulation model for electron transport in CASINO supposes an amorphous specimen (Demers et al., 2011).

The simulations were obtained for an accelerating voltage of 30 kV and a beam diameter of 1 nm. One million electrons trajectories were simulated to decrease the statistical variation inherent of the Monte Carlo method. The Pt nanoparticle diameter in the simulations was 12 nm and was positioned on the above surface of the CNT. The CNT diameter in the simulations was 100 nm with an iron seed cylinder 45 nm long in the center of CNT. The seed radius, which corresponds to the inner void of the CNT, was 12 nm. The transmitted electron ratio was obtained for collection angle between 0 and $\pi/2$ with a step size of 1 mrad. The collection angles were converted to DD using equations (S1) and (S2) with a WD of 6 mm. The contrasts between the different materials were calculated using equation (3). BF-TE and DF-FSED line scans of 5 nm wide T_1 plate and Pt nanoparticle of 5 nm diameter were simulated with a pixel size of 0.40 nm and a probe current of 400 pA. The dwell time was 32.5 µs for the BF-TE line scan and 170 µs for the DF-FSED line scan, which correspond to 81,139 and 423,238 electrons trajectories, respectively. The BF-TE detector angle was 5 mrad and DF-FSED detector angles were 426 and 518 mrad (DD = 19 mm and WD = 6 mm). An image of the 100 nm diameter CNT was simulated with a pixel size of 0.40 nm, a probe current of 400 pA and a pixel dwell time of 170 µs, which correspond to 423,238 electrons per pixel (N_0). For each scan point in the line scan or image, the number of electrons was randomly obtained using a Poisson distribution of N_0 to simulate the effect of gun shot noise on the images (Reimer, 1998; de Jonge et al., 2010; Demers et al., 2011). In the image, Pt nanoparticles with a diameter of 8, 12, and 20 nm were positioned at the top surface of the CNT.

The simulations were repeated for carbon black and titanium dioxide particles. The C particle and the TiO_2 nanoparticles were modeled by a sphere with a diameter of 100 nm for C and between 20 and 200 nm for TiO_2 both without substrate. Here, the particle diameter defines the specimen thickness. The simulations were obtained for an accelerating voltage of 30 kV, a beam diameter of 1 nm, and 1 million electrons.

S4. DF-SED Contrast Simulations

The micrographs in Figure S2a-d were acquired with detector distances of 18.7, 20.7, 25.7, and 30.7 mm, respectively, and with a WD of 5.5 mm (see Table S1 for the corresponding collection angles). The contrast from the simulated micrographs was calculated from the number of transmitted electrons hitting the detector whereas the experimental contrast was calculated with an intensity value between 0 and 255. This intensity is proportional, but not necessary linearly, to the number of transmitted electrons collected by the detector. First, the intensity is affected by detector gain and detector efficiency, which is not directly proportional to the number of detected electrons for a Si diode (Reimer, 1998). Then, the signal from the detector is transformed by the contrast setting, brightness setting, and the conversion to the range 0 and 255 to obtain a micrograph. For this reason, the comparison of the contrast obtained experimentally and by simulations was not possible. However, the variation observed in the contrast values can be compared, but not the absolute magnitude. The contrast was measured between the platinum nanoparticles of diameter d and the carbon nanotube for three diameter ranges: small ($10 < d < 15$ nm), medium (20 < d < 30 nm), and large nanoparticles (d > 30 nm). The carbon intensity values were measured in 7 distinct areas of the nanotube whereas 4, 3 and 3 nanoparticles were used to calculate the contrast for the small, medium and large platinum nanoparticles, respectively. For each diameter range, the mean contrast and standard deviation were calculated and are displayed in Figure S2e.

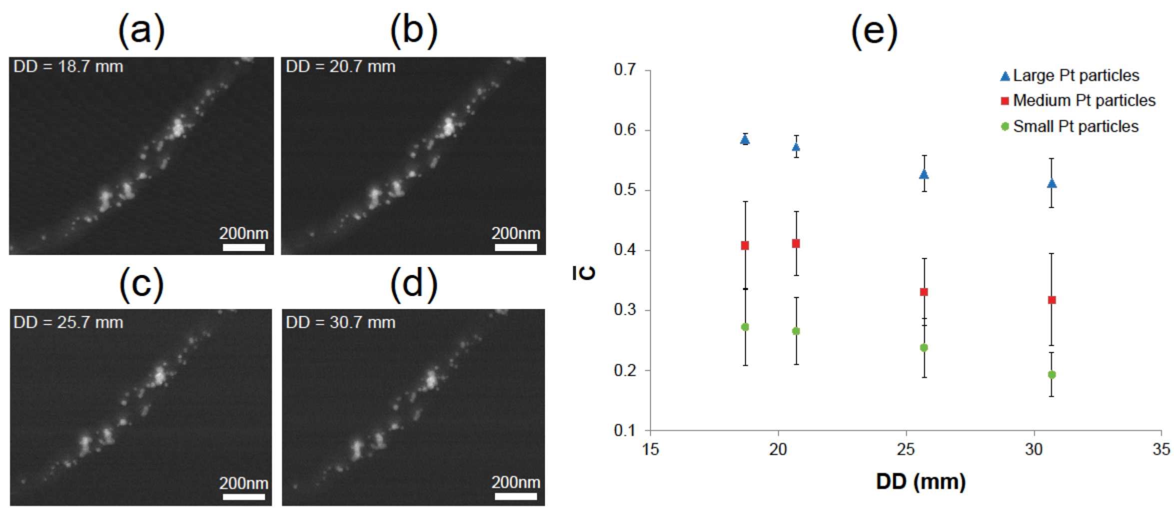

Supplementary Figure S2. Dark-field forescatter electron detector micrographs of carbon nanotubes (CNT) decorated with platinum nanoparticles for different detector distance (DD) illustrating a constant contrast with DD. (a) DD of 18.7 mm (α_1 = 419 mrad), (b) DD of 20.7 mm (α_1 = 468 mrad), (c) DD of 25.7 mm (α_1 = 580 mrad), and (d) DD of 30.7 mm (α_1 = 678 mrad). The working distance was 5.5 mm and the corresponding angles are given in Table 3. (e) The mean contrast ($\overline{C}$) between small (10 < d < 15 nm), medium (20 < d < 30 nm) and large (d > 30 nm) Pt nanoparticles of diameter (d) and the CNT as a function of the DD. Except for large nanoparticles at small DD, the contrast between the CNT and the Pt nanoparticles was unchanged regardless of the DD.

Supplementary Table S1. Minimum (α_1), maximum (α_2) and effective ($\Delta\alpha$) collection angles used in Figure S2 as a function of the detector distance (DD) for a working distance of 5.5 mm calculated with equations (S1) and (S2).

DD (mm)	α_1 (mrad)	α_2 (mrad)	$\Delta\alpha$ (mrad)
18.7	413	505	92
20.7	462	549	87
25.7	573	649	76
30.7	671	737	66

Supplementary References

BEYER, Y., BEANLAND, R. & MIDGLEY, P.A. (2012). Low voltage STEM imaging of multi-walled carbon nanotubes. *Micron* **43** (2-3), 428-434.

DE JONGE, N., POIRIER-DEMERS, N., DEMERS, H., PECKYS, D.B. & DROUIN, D. (2010). Nanometer-resolution electron microscopy through micrometers-thick water layers. *Ultramicroscopy* **110** (9), 1114-1119.

DEMERS, H., POIRIER-DEMERS, N., DROUIN, D. & DE JONGE, N. (2010). Simulating STEM imaging of nanoparticles in micrometers-thick substrates. *Microsc Microanal* **16** (6), 795-804.

DEMERS, H., POIRIER-DEMERS, N., RÉAL COUTURE, A., JOLY, D., GUILMAIN, M., DE JONGE, N. & DROUIN, D. (2011). Three-dimensionnal electron microscopy simulation with the Casino Monte Carlo software. *Scanning* **33** (3), 135-146.

FELISARI, L., GRILLO, V., JABEEN, F., RUBINI, S., MENOZZI, C., ROSSI, F. & MARTELLI, F. (2011). Imaging with low-voltage scanning transmission electron microscopy : a quantitative analysis. *Ultramicroscopy* **111** (8), 1018-1028.

JOY, D.C., KO, Y.U. & HWU, J. (2000). Metrics of resolution and performance for CD-SEMs. *Proc. SPIE* 3998, 108-114.

JOY, D.C. (2002). SMART - a program to measure SEM resolution and imaging performance. *J Microsc* **208**, 24-24.http://link.aip.org/link/doi/10.1117/12.386444

MORANDI, V. & MERLI, P.G. (2007a). Contrast and resolution versus specimen thickness in low energy scanning transmission electron microscopy. *J Appl Phys* **101** (11), 114917.

PROBST, C., DEMERS, H. & GAUVIN, R. (2012). Spatial resolution optimization of backscattered electron images using Monte Carlo simulation. *Microsc Microanal* **18** (3), 628-637.

RASBAND, W.S., ImageJ, U. S. National Institutes of Health, Bethesda, Maryland, USA, http://imagej.nih.gov/ij/, 1997-2012.

REIMER, L. (1998). *Scanning Electron Microscopy – Physics of Image Formation and Microanalysis*, Berlin, New York: Springer.

SALVAT, F., JABLONSKI, A. & POWELL, C.J. (2005). ELSEPA—Dirac partial-wave calculation of elastic scattering of electrons and positrons by atoms, positive ions and molecules. *Comput Phys Commun* **165** (2), 157-190.

WILLIAMS, D.B. & CARTER, C.B. (2009). Part 3: Imaging. In *Transmission Electron Microscopy*, Carter, C.B. & Williams, D.B. (Eds), pp. 369-578. New York: Springer.